Available online at www.sciencedirect.com
ScienceDirect
Journal of Power Sources 160 (2006) 215–223
JOURNAL OF POWER SOURCES
www.elsevier.com/locate/jpowsour

Three dimensional modeling of high temperature PEM fuel cells

Denver F. Cheddie *, Norman D.H. Munroe

Mechanical and Materials Engineering, CEAS 2103, Florida International University, 10555 W. Flagler Street, Miami, FL 33174, United States

Received 17 November 2005; received in revised form 23 December 2005; accepted 5 January 2006
Available online 14 February 2006

Abstract

A three dimensional model of a proton exchange membrane fuel cell (PEMFC) operating with a polybenzimidazole (PBI) membrane is presented. This model is an improvement on the previous three models developed for this type of PEM fuel cell. The model accounts for all transport and polarization phenomena, and the results compare well with published experimental data for the same sets of operating conditions. The model predicts the oxygen depletion, which occurs in the catalyst area under the ribs, and a temperature rise of up to 20 K at a power density of 1000 W m^{-2} can be expected depending on operating conditions.

Keywords: PEM fuel cell; Mathematical modeling; PBI

1. Introduction

Recently there has been a growing interest in high temperature (120–150 °C), low humidity (25–50% RH) proton exchange membrane fuel cells (PEMFCs). The US Department of Energy (DOE) has planned to invest US$ 17.5 million into research in such fuel cells over the next 5 years [1].

Typical PEMFCs, equipped with a Nafion® membrane, operate at temperatures below the boiling point of water (50–80 °C), since Nafion® requires a high water content to effectively conduct protons. To maintain these low temperatures under vehicle driving conditions, especially at peak power, requires over-sized cooling equipment. External humidification is also required to prevent dehydration of the Nafion® membrane, and this adds volume, weight and complexity to the fuel cell system [1].

At higher temperatures, water exists primarily in the vapor phase, so transport limitations associated with the presence of liquid water are precluded. In addition, carbon monoxide (CO) adsorption onto the platinum (Pt) catalyst particles becomes less pronounced at elevated temperatures. Thus, its poisonous effects on fuel cell performance decrease with temperature. Also with high temperature membranes, which are not dependant on water for proton conductivity, external humidification is not required. This reduces overall system cost, weight and size.

Proton exchange membranes fall into three general categories: (1) per-fluorinated ionomer membranes; (2) partially per-fluorinated membranes; (3) non-per-fluorinated membranes [2]. Nafion® is an example of a per-fluorinated ionomer membrane, whereas polybenzimidazole (PBI) is an example of a non-per-fluorinated membrane. PBI was first suggested for use in fuel cells by Wainright et al. [3]. PBI has good mechanical strength, high chemical and thermal stability at high temperatures, and it attains its ionic conductivity when doped with a strong acid such as phosphoric or sulfuric acid. PBI is also highly impermeable to methanol at high temperatures, and has a water drag coefficient of nearly zero, which alleviates cathode flooding and membrane dehydration.

The ionic conductivity of PBI varies significantly depending on temperature, the level of acid doping, method of preparation and composite materials used, if any. Typical conductivity values reported for PBI doped with phosphoric acid range from 0.2 to 6.8 S m^{-1} [3–7]; 5–6 S m^{-1} when doped with sulfuric acid [8,9]; and 9 S m^{-1} when doped with potassium hydroxide [7]. A composite of PBI and ZrP has exhibited a conductivity of 9.6 S m^{-1} [4], while the highest conductivity value reported in the literature is 13 S m^{-1} at 160 °C for PBI doped with 1300–1600 mol% phosphoric acid [7]. There is still a debate over the dependence of PBI conductivity on humidity, whether any such dependence

* Corresponding author. Tel.: +1 786 877 9235; fax: +1 305 348 6142.
E-mail addresses: dcheddie@yahoo.com (D.F. Cheddie), munroen@fiu.edu (N.D.H. Munroe).

0378-7753/$ – see front matter © 2006 Elsevier B.V. All rights reserved.
doi:10.1016/j.jpowsour.2006.01.035

Nomenclature

a	effective surface area (m^{-1})
c_p	specific heat capacity at constant pressure ($J\,kg^{-1}\,K^{-1}$)
$D_{i,j}$	diffusivity of gas pair i–j ($m^2\,s^{-1}$)
D_T	effective thermal diffusivity ($m^2\,s^{-1}$)
F	Faraday constant, 96,487 C mol^{-1}
i	current density ($A\,m^{-2}$)
i_0	exchange current density ($A\,m^{-2}$)
j	reaction rate ($A\,m^{-3}$)
k	thermal conductivity ($W\,m^{-1}\,K^{-1}$)
k_p	gas permeability (m^2)
m	mass fraction
M	molar mass ($kg\,mol^{-1}$)
P	pressure (Pa)
R	universal gas constant, 8.3143 $J\,mol^{-1}\,K^{-1}$
S	source, entropy
T	Temperature (K)
u	velocity ($m\,s^{-1}$)
V	potential (V)
x	mole fraction

Greek letters

α	thermal diffusivity ($m^2\,s^{-1}$), charge transfer coefficient
γ	concentration parameter
ε	porosity
μ	dynamic viscosity (Pa s)
ρ	density ($kg\,m^{-3}$)
σ	electrical or ionic conductivity ($S\,m^{-1}$)
ϕ	electrical or ionic potential (V)

Subscripts

e	electrolyte phase
f	fluid property
i, j	species i, j
m	mass quantity
s	solid phase
T	thermal

Superscripts

d	dispersion
eff	effective

exists, and if so the nature of it [10–12]. PBI has been successfully tested in PEMFCs using hydrogen [8,9,13,14], methanol [15] and other alcohols [16,17]. Maximum power densities are in the order of 1000 W m^{-2} using methanol as the fuel [15] and 4000–9000 W m^{-2} using hydrogen as the fuel [8,9].

Most of the work done in fuel cell modeling over the past 15 years has been for Nafion® membranes [18,19]. The only attempts thus far to model fuel cells equipped with PBI membranes have been conducted by the present authors [20–22]. This paper builds on our previous three models, where we studied 1D and 2D effects. This paper presents a 3D non-isothermal model of a PBI fuel cell. The model describes all transport and polarization phenomena, and accounts for rib effects and the effect of gas channel flow rates. Numerical results for a hydrogen/oxygen and a hydrogen/air fuel cell are compared to the experimental results published by Wang et al. [13].

2. Model development

2.1. Computational domain

Fig. 1 shows the computational domain used in this model, as well as the grid network. In the x-direction, the domain spans the anode gas channel and rib to the cathode gas channel and rib. It includes the membrane electrode assembly (MEA), with catalyst layers treated as finite sized regions, as opposed to vanishing interfaces. In the y-direction, the domain spans half of one channel to half of an adjacent rib. In the work by Wang et al. [13], their fuel cell testing apparatus used five straight gas channels. To simplify the computer memory requirements, analysis was only performed for one channel, symmetry being assumed at the mid-points of each channel and rib. In the z-direction, the domain spans the entire length of the gas channel passing over the active MEA, which is 1 cm × 1 cm in cross section. Thus, the length of the channels in the domain is 1 cm. This dimension is an order of magnitude larger than those in the x- and y-directions. This geometric aspect ratio is not obvious in Fig. 1 for the purpose of making the figure clearer.

2.2. Assumptions

For high temperature fuel cells, water is expected to exist only in the vapor phase; therefore, single phase flow is assumed. Individual gases as well as the gas mixtures are assumed to behave ideally. The porous media and catalyst regions are assumed to be isotropic and macro-homogeneous, and the PBI membrane is assumed to be impermeable to gas flow. Also because of the typically low fluid velocities, the flow is treated as laminar.

The electrochemical reactions are assumed to be gas phase reactions. The present model does not take into account reactant gases dissolving in the electrolyte at the catalyst layer. This would require two-phase modeling, which is the subject of future

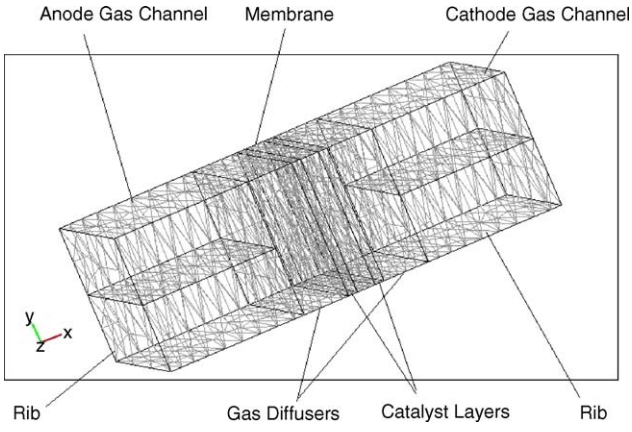

Fig. 1. 3D computational domain and finite element grid.

work. It is expected that a two-phase model, which takes into account gas solubility in the catalyst layers, would be better able to predict mass transport limitations. This model also does not take into account the effect of feed gas humidification on membrane conductivity and electro-kinetic activity, since the mechanisms governing these phenomena are not as yet fully understood.

2.3. Governing equations

$$\nabla \cdot (\rho u) = S_{\mathrm{m}} = \sum S_i \tag{1}$$

The continuity equation (1) has a non-zero term on the RHS, which represents a solid–fluid phase change in the catalyst layers. For a PBI membrane, H^+ ions are transported across the membrane in a solid state via a Grothus mechanism [10–12]. So there is a loss of fluid mass at the anode catalyst layer and a gain in fluid mass at the cathode catalyst layer, as shown in the half cell equations (2) and (3).

$$\mathrm{H_2\,(g)} \rightarrow 2\mathrm{H^+\,(s)} + 2\mathrm{e^-\,(anode)} \tag{2}$$

$$\tfrac{1}{2}\mathrm{O_2\,(g)} + 2\mathrm{H^+\,(s)} + 2\mathrm{e^-} \rightarrow \mathrm{H_2O\,(g)\,(cathode)} \tag{3}$$

Total mass, however, is always conserved at every point; and overall fluid mass is conserved since the H^+, formed at the anode, reconverts to fluid mass at the cathode. But at the catalyst layers, the fluid flow is non-conservative. Across the membrane, the fluid velocity is zero since the PBI membrane is virtually impermeable to gas flow.

The Navier–Stokes equations govern momentum transfer in the gas channels and the electrodes.

$$\rho u \cdot \nabla u = -\nabla P + \nabla \cdot (\mu \nabla u) - \frac{\mu}{k_{\mathrm{p}}} u \tag{4}$$

For the porous diffuser and catalyst regions, the source term corresponding to Darcy's law becomes dominant over the inertia and viscous terms. This source term is non-existent in the gas channels, where the flow is primarily inertial.

Considering that a non-conservative form of the continuity equation is used, the non-conservative Stefan–Maxwell equations must be used for gas species conservation, which were previously derived [21,22].

$$\rho u \cdot \nabla m_i = \nabla \cdot \left[\rho \varepsilon m_i \sum_{j=1}^{N} D_{i,j}^{\mathrm{eff}} \left\{ \frac{M}{M_j} \left(\nabla m_i + m_i \frac{\nabla M}{M} \right) \right\} \right] + S_i - m_i S_{\mathrm{m}} \tag{5}$$

The last term on the RHS accounts for the non-conservative nature of the fluid flow.

The energy equation accounts for convection, conduction and heat generation due to ohmic or Joule heating, as well as heat of reaction.

$$\rho c_p u \cdot \nabla T = \rho c_p \nabla \cdot (D_{\mathrm{T}} \nabla T) + S_{\mathrm{T}} \tag{6}$$

$$S_{\mathrm{T}} = S_{\mathrm{ohm}} + S_{\mathrm{rxn}} \tag{7}$$

The charge conservation equations in the electrolyte and solid phases are given by,

$$\nabla \cdot i_{\mathrm{s}} = \nabla \cdot (-\sigma_{\mathrm{s}}^{\mathrm{eff}} \nabla \phi_{\mathrm{s}}) = -j \tag{8}$$

$$\nabla \cdot i_{\mathrm{e}} = \nabla \cdot (-\sigma_{\mathrm{e}}^{\mathrm{eff}} \nabla \phi_{\mathrm{e}}) = +j \tag{9}$$

$$j = a i_0^{\mathrm{ref}} \left(\frac{x_i P}{P_{\mathrm{ref}}} \right)^{\gamma_i} \left\{ \exp\left[\frac{\alpha F}{RT} (\phi_{\mathrm{s}} - \phi_{\mathrm{e}}) \right] - \exp\left[\frac{(1-\alpha)F}{RT} (\phi_{\mathrm{s}} - \phi_{\mathrm{e}}) \right] \right\} \tag{10}$$

The exchange current density, i_0, is defined in terms of the active catalyst surface area. The effective surface area, a, is defined as the ratio of the total active catalyst surface area to the total catalyst region volume, and thus takes into account surface roughness in the catalyst layer. The Butler–Volmer equation (10) states that the rate of electrochemical reaction is driven by the difference in potential between the two respective phases, and is affected by the concentration of reactants at the catalyst sites. The local reaction rate, j, defines the rate of transfer of solid state current to electrolyte phase current in the anode catalyst layer, and vice versa in the cathode catalyst layer.

2.4. Source terms

The source terms depend on the reaction rate in each catalyst layer and the stoichiometry of the overall cell reaction. With the exception of the ohmic heating term, all other source terms are only non-zero in the catalyst layers. The reaction rate, j, is positive in the anode catalyst layer and negative in the cathode. Thus, the following equations define the local rates of oxygen consumption, water vapor production, hydrogen consumption, reactive heat generation and ohmic heat generation:

$$S_{\mathrm{O_2}} = j \frac{M_{\mathrm{O_2}}}{4F}\ (\mathrm{kg\,m^{-3}\,s^{-1}}) \tag{11}$$

$$S_{\mathrm{H_2O}} = -j \frac{M_{\mathrm{H_2O}}}{2F}\ (\mathrm{kg\,m^{-3}\,s^{-1}}) \tag{12}$$

$$S_{\mathrm{H_2}} = -j \frac{M_{\mathrm{H_2}}}{2F}\ (\mathrm{kg\,m^{-3}\,s^{-1}}) \tag{13}$$

$$S_{\mathrm{rxn}} = -j \left(\phi_{\mathrm{e}} - \phi_{\mathrm{s}} - \frac{T\,\Delta S}{nF} \right)\ (\mathrm{W\,m^{-3}}) \tag{14}$$

$$S_{\mathrm{ohm}} = \frac{i_{\mathrm{s}}^2}{\sigma_{\mathrm{s}}^{\mathrm{eff}}} + \frac{i_{\mathrm{e}}^2}{\sigma_{\mathrm{e}}^{\mathrm{eff}}}\ (\mathrm{W\,m^{-3}}) \tag{15}$$

2.5. Constitutive relations

This section provides a list of constitutive relations necessary to correct the plain media fluid and material properties for the porous media. It also gives the ideal gas relations used in this work. The geometric average of the solid and fluid thermal conductivity is used to determine the effective thermal conductivity

[23].

$$\frac{k^{\text{eff}}}{k_{\text{f}}} = \left(\frac{k_{\text{s}}}{k_{\text{f}}}\right)^{1-\varepsilon} \tag{16}$$

The thermal dispersion diffusivity is given by the following relationship, valid for low Peclet number flows [24]:

$$\frac{D^{\text{d}}}{\alpha_{\text{f}}} = 3(1-\varepsilon)\left(\frac{(k_{\text{s}}/k_{\text{f}})-1}{(k_{\text{s}}/k_{\text{f}})+2}\right) \tag{17}$$

The total effective thermal diffusivity is given by Kaviany [25],

$$\frac{D_{\text{T}}}{\alpha_{\text{f}}} = \frac{k^{\text{eff}}}{k_{\text{f}}} + \frac{\varepsilon D^{\text{d}}}{\alpha_{\text{f}}} \tag{18}$$

This value depends on solid and fluid properties and compositions, as well as porous media characteristics. The effective gas diffusivity is related to the plain media diffusivity [26],

$$\frac{D_{i,j}^{\text{eff}}}{D_{i,j}} = \frac{2\varepsilon}{3-\varepsilon} \tag{19}$$

The electrical and ionic conductivities are corrected for porous media using the Bruggemann correlation [27], where $\varepsilon_{\text{phase}}$ is the volume fraction occupied by the phase through which the respective current flows.

$$\sigma^{\text{eff}} = \sigma\varepsilon_{\text{phase}}^{1.5} \tag{20}$$

The gas mixture (mass) density and molar mass are derived from the ideal gas law.

$$\rho = \frac{PM}{RT} \tag{21}$$

$$M = \left(\sum \frac{m_i}{M_i}\right)^{-1} \tag{22}$$

All other fluid properties are mass averaged for the gas mixture. The plain media gas pair diffusivity is assumed constant at a given temperature and pressure, and independent of composition.

2.6. Boundary conditions

The unified (single domain) approach is used in this model. Thus, boundary conditions are required at the ends of the domain. In the experiments by Wang et al. [13], the feed gases are humidified at 28 °C and supplied to the fuel cell at 150 °C and atmospheric pressure. Their PBI membrane after doping with 5 M phosphoric acid had a thickness 80 μm. They used a commercial E-TEK electrode (0.5 mg cm^{-2} Pt) at the anode, and a home made cathode with 2 mg cm^{-2} Pt loading. They did not, however, report the supply gas flow rates used in their experiments. So in the computations, typical values were used.

In the extremes of the domain in the y-direction, Neumann boundary conditions are specified, since symmetry conditions were assumed in the selection of the domain. In the extremes in the z-direction, the flow inlet and outlet conditions are specified. The overall flow rate is specified at the inlets of each channel, while atmospheric pressure is specified at the outlet. For the species and thermal equations, the concentration and temperature, respectively, are specified at the inlet, while convective flux boundary conditions are specified at the outlets. In the x-direction, insulation conditions are specified for the mass flow and species flow at the membrane/catalyst interfaces since the membrane is impermeable to gas flow. The solid phase potentials are specified at the ribs in the anode and cathode. Zero is chosen as a reference at the anode, while $V_{\text{rev}} - V_{\text{cell}}$ (the difference between the reversible cell potential and the operating cell potential) is specified at the cathode. This quantity represents the total cell polarization. Thus, in this model, the cell potential is stated and the cell current density computed.

3. Results and discussion

The governing equations are solved using FEMLAB® 3.1i, utilizing a finite element method to solve the system of coupled partial differential equations. The computations were performed on a Windows PC with a 1 GB, 3.4 GHz, 32 bit, Pentium 4 processor. The finite element method entailed 3190 second order tetrahedral elements, which for 10 independent variables, constituted a 25,138 degree of freedom problem with a computational error O(h^3). The computational grid is shown in Fig. 1. Computation times were up to 5 min for a single run. A run consists of computing the entire solution for one specified cell voltage. Once this initial solution is obtained, it can be used as an initial guess to compute the solutions for other cell voltages. Subsequent runs take approximately 3 min to solve. Thus, all the data for an *IV* curve can be obtained in approximately 30 min.

This size of grid was considered the best compromise between solution time and accuracy. Fig. 2 shows the tests for grid independence. The variable which showed the most significant variation with grid size was found to be the cell current density, especially at limiting conditions. So this quantity was shown in Fig. 2 versus the number of grid elements. Taking into consideration the scale used in the figure, even coarse grids allowed for an error of less than 0.5%. However, the solution time increased significantly when the grid was refined. A grid consisting of 3190 elements required approximately 5 min of solution time and gave an error of approximately 0.2%, while a grid of 8600 elements required over 20 min of solution time

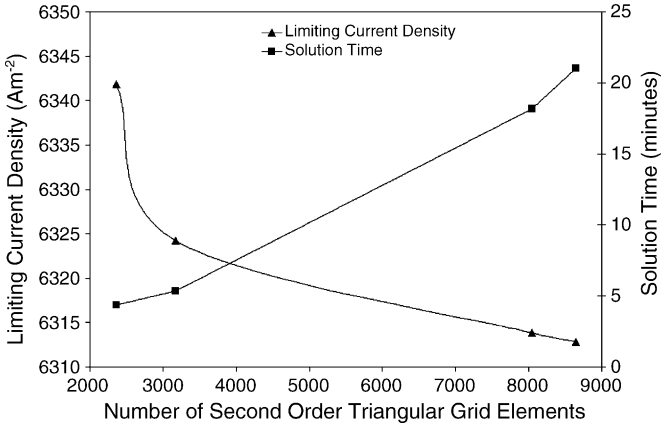

Fig. 2. Grid independence test.

Table 1
Membrane and diffuser properties

Membrane [13]	
Thermal conductivity, k_m (W m^{-1} K^{-1}) [31]	40
Ionic conductivity, σ_m (S m^{-1})	1.87
Thickness (m)	8×10^{-5}
Cross section (m^2)	0.01×0.01
Diffuser (graphite) [28]	
Thermal conductivity, k_d (W m^{-1} K^{-1}) [32]	1.15
Electrical conductivity, σ_d (S m^{-1})	120
Porosity, ε	0.4
Permeability, k_p (m^2)	1.8×10^{-11}
Thickness (m)	2.6×10^{-4}
Channels [13]	
Channel length (m)	0.01
Channel cross section (deduced) (m^2)	0.001×0.001
Rib cross section (deduced) (m^2)	0.001×0.001
Number of channels	5

Table 2
Catalyst layer properties at 423 K

	Anode	Cathode
ai_0^{ref} (A m^{-3}) [30]	10^8	0.02
α [28]	0.5	2
γ [28]	0.5	1
P_{ref} (Pa)	1.013×10^5	
ε (estimated)	0.2	
Fraction of membrane phase in catalyst layer, $\varepsilon_{m,c}$ [28]	0.4	
Catalyst layer thickness (m)	5×10^{-5}	

Table 3
Fluid properties at 423 K [33]

	Oxygen	Nitrogen	Water vapor	Hydrogen
M (kg mol^{-1})	32×10^{-3}	28.16×10^{-3}	18×10^{-3}	2×10^{-3}
k (W m^{-1} K^{-1})	0.036	0.034	0.030	0.239
c_p (J kg^{-1} K^{-1})	956	1050	1980	14500
μ (Pa s)	27×10^{-6}	23×10^{-6}	14×10^{-6}	1.1×10^{-6}
α (m^2 s^{-1})	44.4×10^{-6}	41.0×10^{-6}	30.8×10^{-6}	217×10^{-6}

with only a slight improvement in accuracy. It was concluded that grid independence was attained with 3190 elements.

Tables 1–4 give a list of numerical values used in the computations. The gas diffusers used by Wang et al. [13] are the same as those used for PEMFCs using Nafion®, so the gas diffuser parameters are typical values taken from the literature [28]. In the work of Wang et al. [13], their fuel cell used a MEA of cross section 1 cm^2, as well as flow field containing five straight gas channels. The dimensions of the gas channels and ribs are calculated assuming that the channels are equally spaced and that rib and channel thicknesses are approximately the same. The electrode kinetics data for phosphoric acid doped PBI are reported to be approximately the same as that of pure phosphoric acid [29], so electro-kinetic data for a phosphoric acid fuel cell are obtained from Choudhury et al. [30].

Table 4
Plain media gas pair diffusivities at 423 K and 1 atm [34]

Gas pair	Diffusivity (m^2 s^{-1})
O_2–H_2O	41.9×10^{-6}
O_2–N_2	34.2×10^{-6}
N_2–H_2O	49.2×10^{-6}
H_2–H_2O	144×10^{-6}

3.1. Polarization curves

Fig. 3 shows the polarization curves for both hydrogen/oxygen and hydrogen/air fuel cells. The experimental data are only given by Wang et al. [13] for up to 2500 A m^{-2}, which covers the activation and some of the ohmic regions of the *IV* curve. It is difficult to say, from their data, what limiting current density was observed. However, for the ohmic and activation regions, the model curves match the experimental polarization data well. The model results for air match extremely well with the experimental results. For oxygen, there is a good match except for the last two data points, where the models underestimate the performance. The last two points in the experimental data for oxygen are indeed strange, for it appears as though there is an increase in membrane conductivity as the current density increases. Barring the possibility of this being experimental error (not allowing the cell to fully reach steady state conditions), it is possible that the higher production of water vapor at higher current densities results in increased membrane conductivity, or maybe even enhanced transport characteristics in the catalyst layer leading to more rapid electrode kinetics.

Fig. 3 also shows the effects of varying the inlet gas flow rates on polarization behavior. For the oxygen cell, there is little difference as the flow rate increases from 0.02 to 0.1 L min^{-1}. A flow rate of 0.02 L min^{-1} is not typically used in laboratory fuel cells; nevertheless, it is included in the computation solely for the purpose of comparison. For the air cell, there is little difference in the polarization behavior as the flow rate varies between 0.1 and 1 L min^{-1}; however, the variation is much larger between 0.02 and 0.1 L min^{-1}. The limiting current density over this range varies from approximately 4500 to 6300 A m^{-2}. However, the differences between these two *IV* curves are primarily evident at limiting conditions. This suggests that the air stream is unable to supply oxygen at the required rate for the electrochemical reaction to take place. It can be shown that the rate of consumption

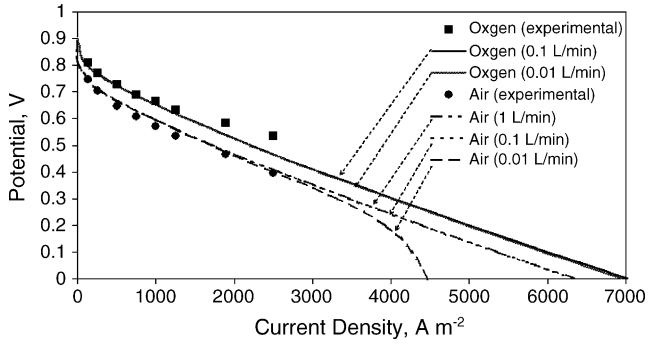

Fig. 3. Current–voltage (*IV*) curves—model predictions and experimental data.

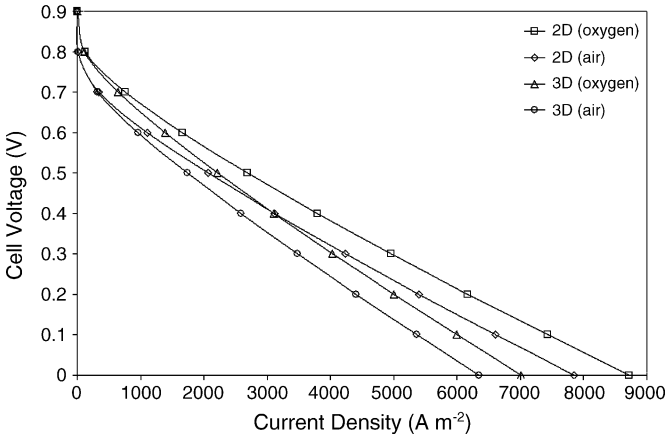

Fig. 4. Comparison of *IV* curves for 3D and 2D [Cheddie] models, flow rate = 3 L min^{-1}.

of oxygen in the electrochemical reaction is given by Eq. (23), from which at 4500 A m^{-2}, the rate of oxygen consumption is 0.04 mg s^{-1}. For an inlet air flow rate of 0.02 L min^{-1}, the mass supply rate of oxygen is 0.06 mg s^{-1}.

$$R_{\text{oxygen}} = \frac{i_{\text{cell}} A_{\text{MEA}} M_{\text{O}_2}}{4F} \tag{23}$$

Thus, the air stream is barely able to supply the necessary oxygen requirement, which results in the distinct concentration overpotential region for this flow rate. But, of note is that this is the only case where a distinct concentration overpotential region is seen. The reason there was no similar concentration region in the other curves is because there is no liquid water at these high temperatures to restrict the flow of reactant gases to the catalyst layer. There may be other factors which result in mass limiting conditions, such as poor reactant transport and kinetics in the catalyst layer. However, this model does not account for such phenomena, neither does the experimental data provide any indication of what are the limiting current densities.

Fig. 4 gives a comparison of the *IV* curve for the present 3D model and our previous 2D model [21] for a common flow rate of 3 L min^{-1}. For the 3D model, the ohmic portions of the *IV* curve have a distinctly steeper gradient, which implied a larger ohmic resistance. The reason for this is that the 3D model accounts for rib effects. The ribs provide an additional contribution to the ohmic overpotential. But also because of the presence of ribs, there is a greater mean electron path, meaning that the current must flow through a slightly greater distance to reach the ribs, than if the ribs were not present. This results in a further ohmic potential drop. So the combination of both effects results in a greater overall cell resistance. The consequence is a smaller limiting current density predicted by the 3D models. The differences in limiting current density predicted by 2D and 3D models are between 1000 and 2000 A m^{-2}. The presence of ribs also results in areas of oxygen depletion, which results in slower electrode kinetics. However, this did not appear to have a significant effect on the *IV* curves. The major difference between the 2D and 3D curves appears to be ohmic in nature.

3.2. Transport characteristics

Oxygen depletion is a problem, which occurs when air is used as the oxidant because of its lower oxygen content than that of pure oxygen. Figs. 5 and 6 show the oxygen mass fraction variations in the cathode region for two flow rates, 1.0 and 0.1 L min^{-1}, respectively. These figures apply at limiting conditions (zero cell voltage), and for humidified air as the oxidant. It shows that concentration effects are more pronounced at lower flow rates. For both flow rates, there is a region of low oxygen concentration in the catalyst layer under the ribs. There is a general decrease in concentration in the negative *x*-direction, since oxygen must diffuse against the bulk flow. There is also a concentration decrease in the negative *y*-direction due to the presence of the ribs. Oxygen must travel a greater distance to diffuse from the channels to the area under the ribs. This oxygen depletion is a slightly more pronounced at the lower flow rate, and results in slow reaction kinetics and ineffective catalyst utilization. However, the biggest difference between the two flow rates occurs in the *z*-direction. There is a greater variation in oxygen concentration along the gas channel in the direction of flow (positive *z*-direction). For the lower flow rate, a larger

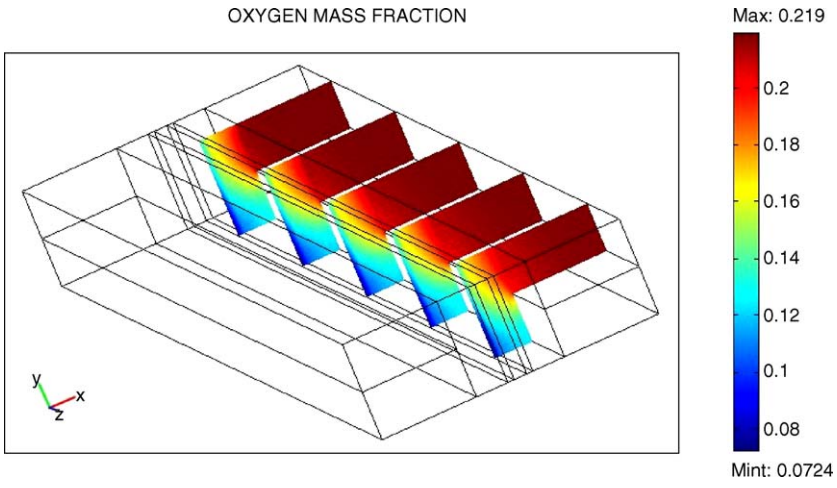

Fig. 5. Oxygen mass fraction for the humidified hydrogen/air cell, flow rate = 1 L min^{-1}.

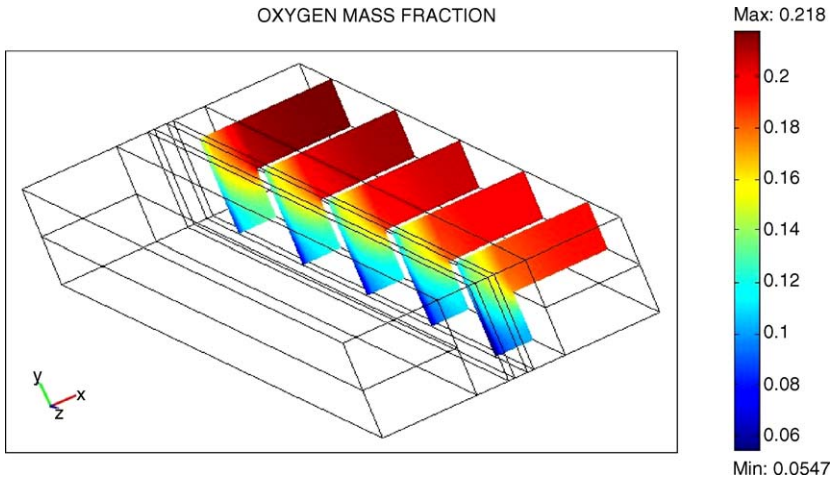

Fig. 6. Oxygen mass fraction for the humidified hydrogen/air cell, flow rate = 0.1 L min^{-1}.

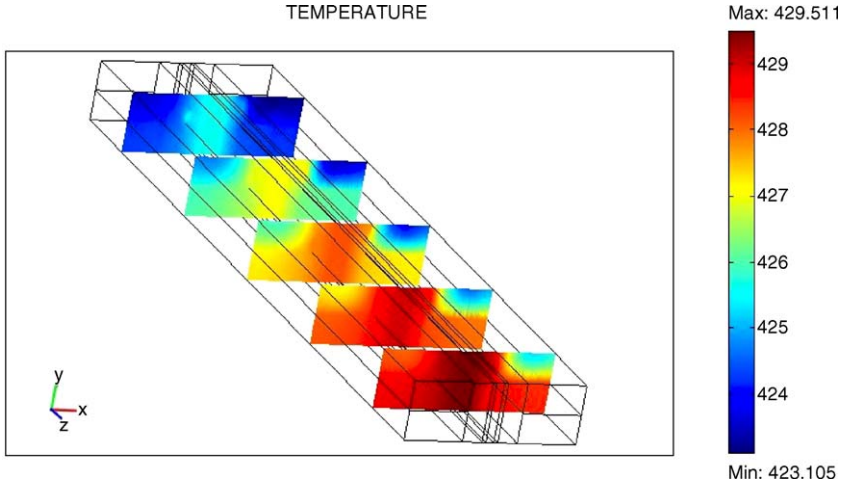

Fig. 7. Temperature (K) variation for the humidified hydrogen/air cell, flow rate = 1 L min^{-1}.

fraction of oxygen is consumed in the electrochemical reactions. The result is a visible decrease in oxygen mass fraction along the channel at the lower flow rate (Fig. 6). This variation is not as visible at the higher flow rate (Fig. 5).

Figs. 7 and 8 show the temperature variations in the cell for the same two flow rates mentioned above. These pertain to the air cell operating at a cell voltage of 0.4 V, which is close to optimum operation. They show a temperature varia-

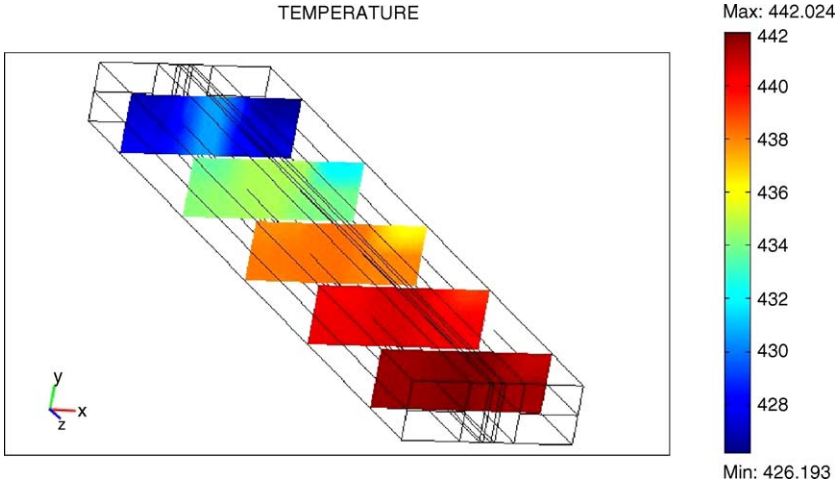

Fig. 8. Temperature (K) variation for the humidified hydrogen/air cell, flow rate = 0.1 L min^{-1}.

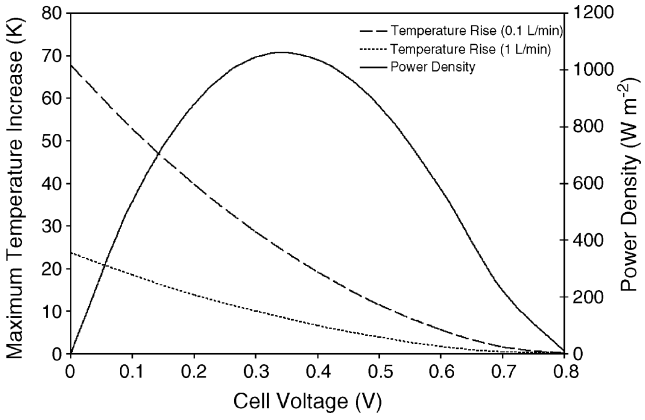

Fig. 9. Temperature variation and power density vs. cell voltage.

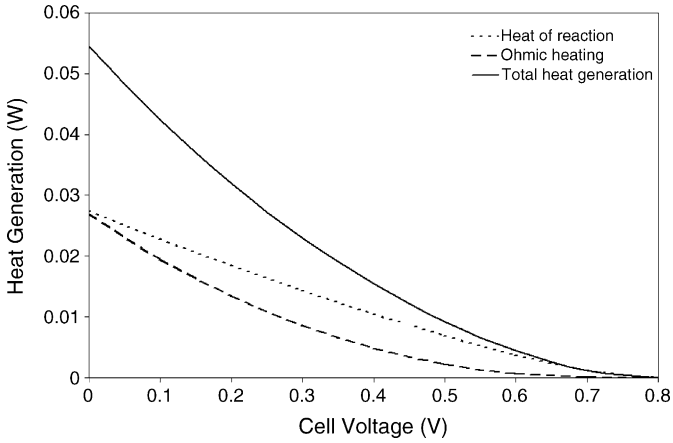

Fig. 10. Ohmic and reactive heat generation vs. cell voltage.

tion in the cell of 7 and 19 K, respectively, the smaller variation for the higher flow rate. From a simple mass balance calculation, it can be shown that such temperature variations are expected. The volumetric heat capacity in both channels is approximately 1000 J m^{-3} K^{-1}. The total heat generation for the conditions represented in Figs. 7 and 8 is 0.015 W for the computational domain (0.077 W for the entire fuel cell unit, recalling that there are five gas channels). This heat generation was obtained from the software by integrating the local heat generations over the entire computational domain. For flow rates of 1.0 and 0.1 L min^{-1}, the expected temperature "pick up" by the gas streams are expected to be approximately 2 and 20 K, respectively. This is consistent with the temperatures in the gas channels shown in Figs. 7 and 8.

Fig. 7 (and to a less visible extent, Fig. 8) shows that there are temperature variations in all three co-ordinate directions. The z-direction variation is the result of heat being absorbed by the gas streams. The heat produced in the fuel cell is transported, via convection, by the flow gases. The x-direction variation is due to the low ionic conductivity of the PBI membrane compared to the gas diffusion electrodes. This results in higher ohmic heating in the membrane. There is also heat produced, which is assumed to be greatest in the cathode catalyst layer. This heat must flow out of the MEA in the x-direction, resulting in a temperature variation in this direction, with the hot points occurring close to the membrane. The most significant y-direction variation is seen where the gas channels and the ribs meet. There is ohmic heating in the ribs, and negligible heat generation in the channels. As a result, the ribs attain a higher temperature than the channel bulk flow.

These results were shown for a cell voltage of 0.4 V. Fig. 9 shows the variation of maximum temperature variation versus cell voltage for the two flow rates of interest. The figure also shows the power density variation, which peaks between 0.3 and 0.4 V. The power density is not significantly different for the two flow rates, so only one curve is shown. The temperature variation increases exponentially as limiting conditions approach (cell voltage tends to zero), where temperature increases of 20–70 K are expected. The reason for this is that as the cell voltage decreases, the current density increases resulting in greater ohmic heating. The heat of reaction also increases due to increasing irreversibilities as the cell tends away from open circuit conditions. Fig. 10 shows the variation of ohmic and reactive heat generations with cell voltage. Once again, these graphs are not significantly affected by flow rate in the range 0.1–1.0 L min^{-1}. If there were a more pronounced concentration overpotential region in the IV curve, then the rate of increase of current with voltage would decrease sharply at limiting conditions, and hence the ohmic heating contribution would be less than those shown in Fig. 10. This would result in lower temperatures at limiting conditions, than those predicted in Fig. 8. Nevertheless, it is not desirable to run the fuel cell close to limiting conditions. At optimum conditions, the temperature variations are much more manageable.

4. Conclusions

A three dimensional mathematical model of a PEM fuel cell equipped with a PBI membrane was developed. The model accounted for all transport phenomena and polarization effects. Its predictions match well with experimental results published by Wang et al. [13]. Compared to a previously developed two-dimensional model, the 3D model predicted a greater ohmic contribution due to the presence of ribs, which result in a decrease in IV characteristics. In other words, the 2D model overestimated the performance by neglecting rib effects.

Results show that the greatest area of oxygen depletion occur in the cathode catalyst layer just under the ribs. This depletion increases in the direction of flow, and is more prominent at lower supply gas flow rates. The temperature increases in the cell in the direction of the channel flow, as expected, since heat generated is absorbed by the feed gases. The hottest points occur in the membrane just under the ribs. This is close to the region of greatest ohmic and reactive heating. The temperature variation across the cell ranges from 7 to 19 K at optimum conditions. At limiting conditions, much higher temperature variations are predicted.

This model did not take into account reactant gas solubility at the catalyst layers, since it assumed gas phase reactions. Taking this phenomenon into account, as well as dissolved gas kinet-

ics, may render the model better able to predict mass limitation effects. This is the subject of future work.

Acknowledgements

The authors are grateful for the FIU Graduate School Dissertation Fellowship, and to Gas Technology Institute (Contract Number 8390) for their support of this work.

References

[1] DOE, High Temperature, Low Relative Humidity Polymer Type Membranes: DE-PS36-05GO95020, Retrieved October 29, 2005, from http://www.eere.energy.gov/hydrogenandfuelcells/program_solicitations.html.
[2] O. Savadogo, Emerging membranes for electrochemical systems. Part II. High temperatures composite membranes for polymer electrolyte fuel cell (PEFC) applications, J. Power Sources 127 (2004) 135–161.
[3] J.S. Wainright, J.T. Wang, D. Weng, R.F. Savinell, M. Litt, Acid-doped polybenzimidazoles: a new polymer electrolyte, J. Electrochem. Soc. 142 (1995) L121.
[4] R. He, Q. Li, G. Xiao, N.J. Bjerrum, Proton conductivity of phosphoric acid doped polybenzimidazole and its composites with inorganic proton conductors, J. Membr. Sci. 226 (2003) 169–184.
[5] P. Staiti, M. Minutoli, Influence of composition and acid treatment on proton conduction of composite polybenzimidazole membranes, J. Power Sources 94 (2001) 9–13.
[6] J.J. Fontanella, M.C. Wintersgill, J.S. Wainright, R.F. Savinell, M. Litt, High pressure electrical conductivity studies of acid doped polybenzimidazole, Electrochim. Acta 43 (1998) 1289–1294.
[7] Q. Li, H.A. Hjuler, N.J. Bjerrum, Phosphoric acid doped polybenzimidazole membranes: physiochemical characterization and fuel cell applications, J. Appl. Electrochem. 31 (2001) 773–779.
[8] B. Xing, O. Savadogo, Hydrogen/oxygen polymer electrolyte membrane fuel cells (PEMFCs) based on alkaline-doped polybenzimidazole (PBI), Electrochem. Commun. 2 (2000) 697–702.
[9] B. Xing, O. Savadogo, Hydrogen/oxygen polymer electrolyte membrane fuel cell (PEMFC) based on acid-doped polybenzimidazole (PBI), J. New Mater. Electrochem. Syst. 3 (2000) 345–349.
[10] H. Pu, W.H. Meyer, G. Wegner, Proton transport in polybensimidazole blended with H_3PO_4 or H_2SO_4, J. Polym. Sci.: Part B: Polym. Phys. 40 (2002) 663–669.
[11] R. Bouchet, E. Siebert, Proton conduction in acid doped polybenzimidazole, Solid State Ionics 118 (1999) 287–299.
[12] R. Bouchet, S. Miller, M. Duclot, J.L. Souquet, A thermodynamic approach to proton conductivity in acid-doped polybenzimidazole, Solid State Ionics 145 (2001) 69–78.
[13] J.T. Wang, R.F. Savinell, J.S. Wainright, M. Litt, H. Yu, A H_2/O_2 fuel cell using acid doped polybenzimidazole as polymer electrolyte, Electrochim. Acta 41 (1996) 193–197.
[14] Q. Li, J. He, A. Gao, J. Jensen, N. Bjerrum, The CO poisoning effect in PEMFCs operational at temperatures up to 200 °C, J. Electrochem. Soc. 150 (2003) A1599–A1605.
[15] J.T. Wang, J.S. Wainright, R.F. Savinell, M. Litt, Direct methanol fuel cell using acid-doped polybenzimidazole as polymer electrolyte, J. Appl. Electrochem. 26 (1996) 751–756.
[16] J. Wang, S. Wasmus, R. Savinell, Evaluation of ethanol, 1-propanol, and 2-propanol in a direct oxidation polymer–electrolyte fuel cell. A real-time mass spectrometry study, J. Electrochem. Soc. 142 (1995) 4218–4225.
[17] Q. Li, H. Hjuler, C. Hasiotis, J. Kallitsis, C. Kontoyannis, N. Bjerrum, A quasi-direct methanol fuel cell system based on blend polymer membrane electrolytes, Electrochem. Solid-State Lett. 5 (2002) A125–A128.
[18] D. Cheddie, N. Munroe, Review and comparison of approaches to PEMFC modeling, J. Power Sources 147 (2005) 72–84.
[19] C.Y. Wang, Fundamental models for fuel cell engineering, Chem. Rev. 104 (2004) 4727–4766.
[20] D. Cheddie, N. Munroe, Mathematical model of a PEMFC using a PBI membrane, Energy Convers. Manage., in press.
[21] D. Cheddie, N. Munroe, Parametric model of an intermediate temperature PEMFC, J. Power Sources, in press.
[22] D. Cheddie, N. Munroe, Two dimensional phenomena in intermediate temperature PEMFCs, Int. J. Transport Phenom., in press.
[23] G.R. Hadley, Thermal conductivity of packed metal powders, Int. J. Heat Mass Transfer 29 (1986) 909–920.
[24] D.L. Koch, J.F. Brady, Dispersion in fixed beds, J. Fluid Mech. 154 (1985) 399–427.
[25] M. Kaviany, Principles of Heat Transfer in Porous Media, Springer-Verlag, NY, 1991.
[26] G.H. Neale, W.K. Nader, Prediction of transport processes within porous media: diffusive flow processes within homogeneous swarm of spherical particles, AIChE J. 19 (1973) 112–119.
[27] R.E. Meredith, C.W. Tobias, Conduction in heterogeneous systems, in: C.W. Tobias (Ed.), Advances in Electrochemistry and Electrochemical Engineering, vol. 2, Interscience Publishers, NY, 1962.
[28] D.M. Bernardi, M.W. Verbrugge, A mathematical model of the solid-polymer–electrolyte fuel cell, J. Electrochem. Soc. 139 (1992) 2477–2491.
[29] Z. Liu, J. Wainright, R. Savinell, High-temperature polymer electrolytes for PEM fuel cells: study of the oxygen reduction reaction (ORR) at a Pt-polymer electrolyte interface, Chem. Eng. Sci. 59 (2004) 4833–4838.
[30] S. Choudhury, M. Deshmukh, R. Rengaswamy, A two-dimensional steady-state model for phosphoric acid fuel cells (PAFC), J. Power Sources 112 (2002) 137–152.
[31] Boedeker Plastics, Inc., Celazole® PolyBenzImidazole Specifications, Retrieved June 15, 2005, from http://www.boedeker.com/celazo_p.htm.
[32] Properties for Graphite, University of California, San Diego (UCSD), Retrieved June 15, 2005, from http://casl.ucsd.edu/data_analysis/carpet_plots.htm.
[33] K. Wark, K. Wark Jr., Advanced Thermodynamics for Engineers, McGraw Hill, NY, 1994.
[34] J.R. Welty, C.E. Wicks, R.E. Wilson, Fundamentals of Momentum. Heat and Mass Transfer, Wiley, NY, 1969.